Retention of Electronic Conductivity in $LaAlO_3/SrTiO_3$ Nanostructures Using a $SrCuO_2$ Capping Layer

P. P. Aurino,[1,*] A. Kalabukhov,[1] R. Borgani,[2] D. B. Haviland,[2] T. Bauch,[1] F. Lombardi,[1] T. Claeson,[1] and D. Winkler[1]

[1]*Department of Microtechnology and Nanoscience—MC2, Chalmers University of Technology, SE-412 96 Gothenburg, Sweden*

[2]*Department of Nanostructure Physics, KTH Royal Institute of Technology, SE-106 91 Stockholm, Sweden*

(Received 14 April 2016; revised manuscript received 17 June 2016; published 12 August 2016)

The interface between two wide band-gap insulators, $LaAlO_3$ and $SrTiO_3$ (LAO/STO) offers a unique playground to study the interplay and competitions between different ordering phenomena in a strongly correlated two-dimensional electron gas. Recent studies of the LAO/STO interface reveal the inhomogeneous nature of the 2DEG that strongly influences electrical-transport properties. Nanowires needed in future applications may be adversely affected, and our aim is, thus, to produce a more homogeneous electron gas. In this work, we demonstrate that nanostructures fabricated in the quasi-2DEG at the $LaAlO_3/SrTiO_3$ interface, capped with a $SrCuO_2$ layer, retain their electrical resistivity and mobility independent of the structure size, ranging from 100 nm to 30 μm. This is in contrast to noncapped LAO/STO structures, where the room-temperature electrical resistivity significantly increases when the structure size becomes smaller than 1 μm. High-resolution intermodulation electrostatic force microscopy reveals an inhomogeneous surface potential with "puddles" of a characteristic size of 130 nm in the noncapped samples and a more uniform surface potential with a larger characteristic size of the puddles in the capped samples. In addition, capped structures show superconductivity below 200 mK and nonlinear current-voltage characteristics with a clear critical current observed up to 700 mK. Our findings shed light on the complicated nature of the 2DEG at the LAO/STO interface and may also be used for the design of electronic devices.

DOI: 10.1103/PhysRevApplied.6.024011

I. INTRODUCTION

The research of new material systems is motivated by the need for electronic devices with lower power consumption, higher speed, and greater design flexibility with devices made from environmentally benign compounds. Complex metal oxides are actively sought in the next generation of electronic devices. Polar oxide interfaces may become key elements of future electronics, and their incorporation into existing or novel electronic platforms requires a deep knowledge about their fundamental properties, which are largely governed by strongly correlated electronic interaction effects. The polar interface between $LaAlO_3$ (LAO) and $SrTiO_3$ (STO) has been intensively studied during the past ten years. A remarkable feature of this interface is the high-mobility quasi-two-dimensional electron gas (q2DEG) that is formed when at least 4 unit cells (u.c.) of LAO are epitaxially deposited on STO under specific conditions [1]. This q2DEG shows unique properties [2,3], such as two-dimensional superconductivity [4,5], a giant electric-field effect [6], and the possible coexistence of ferromagnetic and superconducting phases [7].

Several studies focus on the electrical-transport properties of this interface at the nanoscale [8,9]. Independent works report evidence of inhomogeneity of the q2DEG, based on both the electrical-transport distribution and the presence of ferromagnetic patches in a uniform paramagnetic background [10–12]. Such an electronic phase separation may strongly affect the conductivity of nanowires formed in the two-dimensional sheet. Monte Carlo simulations show that oxygen-vacancy defects may form clusters and "ferromagnetic puddles" spatially separated from superconducting areas [13]. A recent theoretical study [14] proposes a more complex model with a separation into two electronic phases, one with high-mobility carriers and the other with low-mobility carriers. Moreover, the density of the low-mobility carriers is found to be much larger than that of high-mobility carriers, leading to the formation of superconducting "superpuddles" in the high-mobility areas that grow with decreasing temperature to form a percolative network within a weakly localized metallic matrix. Isolated superconductivity may exist in the puddles even before they make contact and form a globally coherent state. This inhomogeneity may also explain the observations of a pseudogap [15,16] in the LAO/STO interfaces. The effect of inhomogeneous electrical transport is most pronounced in structures having a width comparable to the average size

*Corresponding author.
aurino@chalmers.se

of the puddles estimated from scaling arguments to be on the order of 100 nm [17].

We show in a previous work [18] that it is possible to pattern nanostructures into the LAO/STO interfacial q2DEG down to 50 nm using low-energy Ar^+ ion-beam irradiation, combined with optical or *e*-beam lithography. We also find that the room-temperature sheet resistance is approximately constant for structures with a width above 1 μm; below 1 μm, an increase of the sheet resistance is observed. Electrical inhomogeneity of the q2DEG is a possible explanation of this increase of sheet resistance in nanostructures. Moreover, a significant irreproducibility in the sheet resistance of nanopatterned structures is noted at a low temperature; most of them show nonmetallic behavior and resistance increases above the measurement limit (20 GΩ) with a decreasing temperature below 10 K.

Recently, it was shown [19] that adding a $SrCuO_2$ (SCO) capping layer, on the top of the LAO film, improves the conductivity of the q2DEG. The interpretation is that the capping layer helps to fill oxygen vacancies in the STO substrate, resulting in a reduced scattering of carriers at the interface. It is shown that 1 u.c. of SCO is enough to increase the electrical conductivity and mobility by one order of magnitude. Such SCO-capped samples show a constant carrier density over a wide range of temperatures, in contrast to the usual noncapped LAO/STO samples, which show a temperature dependence of the carrier density. Finally, no evidence of superconductivity in the SCO-capped LAO/STO interface is presented [19].

In this work, we study electrical-transport properties in nanostructured LAO/STO interfaces, both uncapped and capped with an SCO layer. We observe that the SCO capping layer indeed improves the electrical conductivity of LAO/STO samples at a macroscopic scale, but it also changes the characteristics of the interface at the nanoscale. Nanostructures patterned in the SCO-capped LAO/STO show sheet resistance, charge-carrier density, and electron mobility comparable to that measured in micrometer-size structures on the same samples, in contrast to the size dependence observed for noncapped samples. Intermodulation electrostatic force microscopy reveals an inhomogeneous surface potential in both capped and noncapped interfaces, with a much smaller variation in the surface potential observed in the capped samples. Moreover, SCO-capped nanostructures show superconducting transitions, in contrast to what is reported in Ref. [19].

II. METHODS

We use 1-u.c.-thick SCO and 2-u.c.-thick STO as capping layers using a similar fabrication process to that which is shown to be optimal for improving the electrical properties of the LAO/STO interface, according to Ref. [19]. The thickness of the LAO film is set to 6 u.c., thus giving a total thickness of the heterostructures of 9 u.c. Thin films are grown on 5×5 mm^2 large TiO_2-terminated STO [20,21] substrates by pulsed laser deposition [22]. The laser energy density is 1.5 J/cm^2, and the laser spot area on the target is 2 mm^2. The sample is heated to 850 °C, and 6 u.c. of LAO are deposited in an oxygen atmosphere of 10^{-4} mbar. The temperature is subsequently decreased to 650 °C, and 1 u.c. of SCO is deposited at an oxygen pressure of 6×10^{-2} mbar. Finally, at the same pressure and temperature, 2 u.c. of STO are deposited as a protecting layer, and the sample is slowly cooled down to room temperature under deposition pressure. The 6 u.c. of LAO are needed to get a conducting interface when LAO is capped by SCO/STO, not 4 u.c. as is the case for uncapped LAO. Following the recipe reported in Ref. [19], the samples are not (conventionally) annealed in oxygen at 500 °C. However, we postanneal a capped sample in a separate experiment and find a significant decrease in the conductivity, casting some doubt on the oxygen-vacancy-filling model suggested [19]. The deposition process is monitored using *in situ* reflection high-energy electron diffraction (RHEED) [23]. Intensity oscillations confirm a layer-by-layer growth [24]. All the samples are inspected by an atomic force microscope (AFM, Bruker Dimension ICON, tapping-mode height image) to confirm the smoothness of the surfaces and the presence of 1-u.c.-high step terraces. In the following, we refer to samples with SCO/STO capping layers as SCO capped.

Patterning of the q2DEG is performed using a low-energy ion-beam irradiation technique [18]. An etch mask is patterned by *e*-beam lithography (JEOL JBX-9300FS) in negative resist (MicroResist maN2401). The sample is then irradiated by an Ar ion beam in an Oxford IonFab 300 Plus system using an inductively coupled plasma Ar^+ source and a 3-cm beam aperture. The irradiation time is 1 min, with a beam energy of 150 eV and a current density of 0.03 mA/cm^2. We have previously reported that the time required to induce the metal-insulator transition depends on the LAO-layer thickness [25]. We use a similar process to irradiate the SCO-capped samples and find that this time is independent of the composition of the capping layer as long as the total thickness is comparable [24]. Electrical connections are provided by dc magnetron sputtering of 20 nm titanium and 120 nm gold contact pads with a standard liftoff process.

Nano Hall bars, nanorings, and macroscopic Hall bars are patterned in the q2DEG. Nano Hall bars have a fixed width of 100 nm and are fabricated with different segment lengths of 200, 400, and 700 nm. Nanorings have a fixed aspect ratio between the width and internal diameter of 1:4 and widths down to 100 nm. For comparison, macroscopic Hall bars are fabricated with a linewidth of 30 μm and a 200-μm segment length. All the electrical measurements from room temperature down to 2 K are performed in a physical properties measurement system (Quantum Design). The low-temperature measurements (down to

20 mK) are performed in a helium dilution cryostat (Oxford Triton 200).

Surface potential imaging is acquired using intermodulation electrostatic force microscopy (ImEFM, Intermodulation Products) [26]. ImEFM is an alternative to Kelvin probe force microscopy, which uses resonance to enhance the force sensitivity of the cantilever (MikroMasch HQ:NSC15/Pt), allowing for a much improved signal-to-noise ratio in a given measurement bandwidth (inverse of the signal integration time at each pixel). The single-pass method works without voltage feedback to create an image of the contact potential difference or the difference between the work function of the surface and that of the Pt tip, $V_{CPD} = \Phi_{surface} - \Phi_{tip}$. The AFM tip works very close to the surface, resulting in a high spatial resolution.

III. RESULTS

Figure 1 shows tapping-mode AFM images of a 200-nm-segment-length nano Hall bar and a 100-nm nanoring. The image shows that the structures are well defined and the effective dimensions correspond to the expected ones. The height difference between irradiated (darker) and nonirradiated (brighter) areas is less than 1 nm as expected from our previous results [18].

The room-temperature sheet resistance as a function of the linewidth for nano Hall bars and macroscopic Hall bars, both fabricated in SCO-capped LAO/STO, are shown in Fig. 2. For comparison, similar data from noncapped structures are also shown [18]. It is evident that the sheet resistance in the SCO-capped structures is reduced by at least a factor of 10 as compared to noncapped, in agreement with results presented in Ref. [19]. It is also clear that the sheet resistance in the capped nanostructures is comparable to that measured in wider structures. In contrast, the noncapped LAO/STO shows a significant increase of sheet resistance when the structure size is smaller than 1 μm.

The temperature dependences of the sheet resistance, carrier concentration, and Hall mobility of the nanoscale

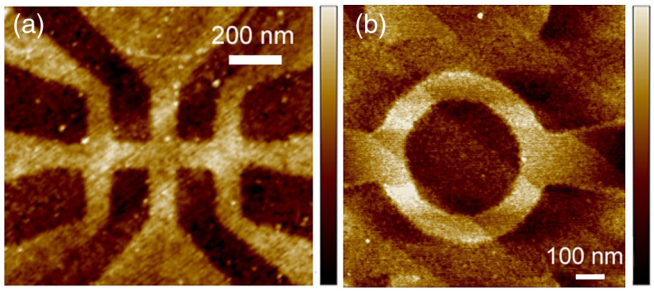

FIG. 1. AFM height images of two nanostructures patterned in the SCO-capped LAO/STO interface using Ar^+ ion-beam irradiation: (a) Hall bar with a nominal linewidth of 100 nm and segment length of 200 nm and (b) ring with a nominal linewidth of 100 nm and inner diameter of 400 nm. In both figures, the color scale ranges between −1 and 1 nm.

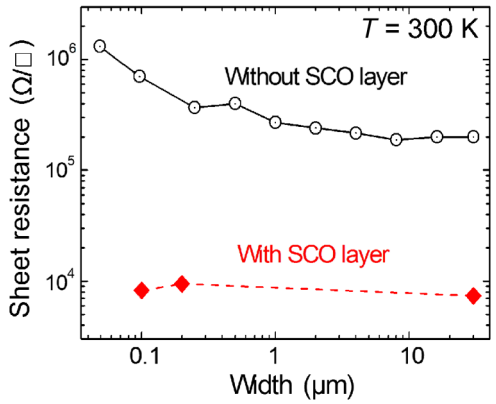

FIG. 2. Sheet resistance measured at room temperature in different structures patterned with a SCO capping layer (diamonds) and without (circles) as a function of their linewidth.

and macroscopic Hall bars made from a capped LAO/STO interface are presented in Fig. 3. The electrical-transport properties are very similar in both structures irrespective of the scale. We measure several different structures, and all show similar behavior. However, it appears that the carrier concentration in our samples shows a stronger temperature dependence than that of Ref. [19], where the carrier concentration is almost independent of the temperature for a sample prepared under similar conditions to ours.

ImEFM images of nanoring structures with a linewidth of 300 nm are presented in Figs. 4(a)–4(e). In both noncapped [Fig. 4(a)] and capped [Fig. 4(b)] structures, one can clearly resolve the conducting ring from the insulating surrounding; however, the contrast, or change in the contact potential difference, is much larger in the noncapped structure. Figure 4(c)) shows histograms of the images in Figs. 4(a) and 4(b), where one can see that the noncapped structure has both a lower V_{CPD} over the insulating region and a higher V_{CPD} over the conducting regions. Assuming that the Pt tip has a fixed work function, we can conclude that capping results in both an increase of the work function in the insulating region and a decrease in the conducting region. We also note that the noncapped structure shows a distinct difference in V_{CPD} between the conducing leads (ring) and the conducting gate electrodes. This difference may be due to the fact that the leads of the device are grounded during the measurement, whereas the gate is left floating.

Figures 4(d) and 4(e) show higher-resolution scans over the conducting lead region of both noncapped and capped samples, respectively. One can clearly see the granularity of V_{CPD}, which we analyze by calculating the radial autocorrelation function (ACF), plotted in Fig. 4(f). The rapid decay of the ACF at a low distance is due to noise, whereas the first peak at a larger distance gives the correlation length for variation in V_{CPD}, or the characteristic size of the puddles. The capped sample has a smoother ACF,

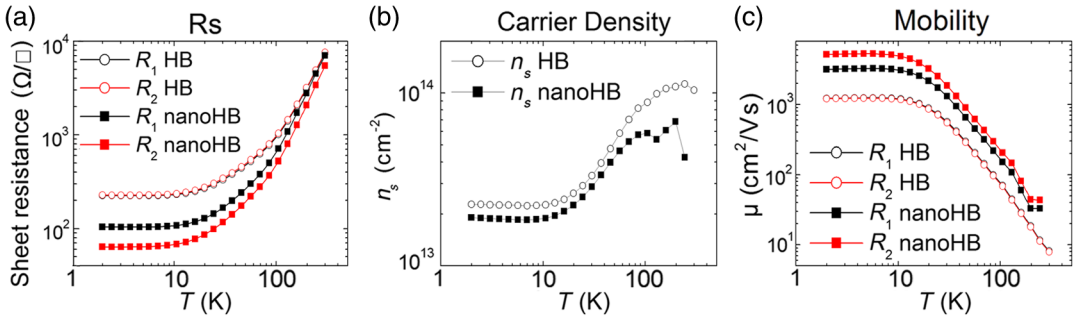

FIG. 3. Electrical-transport properties of macro (HB) and nano Hall bars (nanoHB) patterned in a SCO-capped LAO/STO interface. Temperature dependence of the (a) sheet resistance, (b) carrier density, and (c) mobility, for nanostructures (solid squares) and macroscopic structures (empty circles). The sheet resistance and mobility represent data for two different segments on the same Hall bar (black and red). Both structures are fabricated on the same sample.

indicating a more homogeneous material. In contrast, the noncapped sample shows a larger variation of the ACF at a length scale around 130 nm. These variations in the ACF may explain why the measured resistivity of the noncapped samples increases when their transverse dimensions become of the order of this correlation length scale.

SCO-capped structures show superconducting transitions below 300 mK. A set of current-voltage characteristics for a ring with a linewidth of 100 nm is shown in Fig. 5(a). From the critical current dependence on the temperature shown in Fig. 5(b), the critical temperature can be estimated to about 280 mK for a ring and 200 mK for a wire of the same width (100 nm). Furthermore, the conductance as a function of the voltage [Fig. 5(c)] shows the persistence of a nonlinear behavior above the superconductive transition, resulting in the long "tails" in the estimation of the critical current [see Fig. 5(b)].

IV. DISCUSSION

Our results show that the SCO capping layer significantly improves the electrical-transport properties of the q2DEG at the LAO/STO interface at the nanoscale. The sheet resistance is reduced by a factor of 10 as compared with the noncapped interface. The Hall mobility is also increased, even if we do not reach as high values as reported in Ref. [19]. The carrier concentration of our samples significantly decreases with a decreasing temperature, in contrast to the temperature-independent behavior reported in Ref. [19], where a temperature-independent carrier concentration is used to support an oxygen-vacancy-scavenging scenario. While we follow exactly the same recipe for sample fabrication as in Ref. [19], a minor variation in the oxygen pressure or laser energy density during film growth may result in residual oxygen vacancies or other defects, e.g., Sr/La and Ti/Al intermixing,

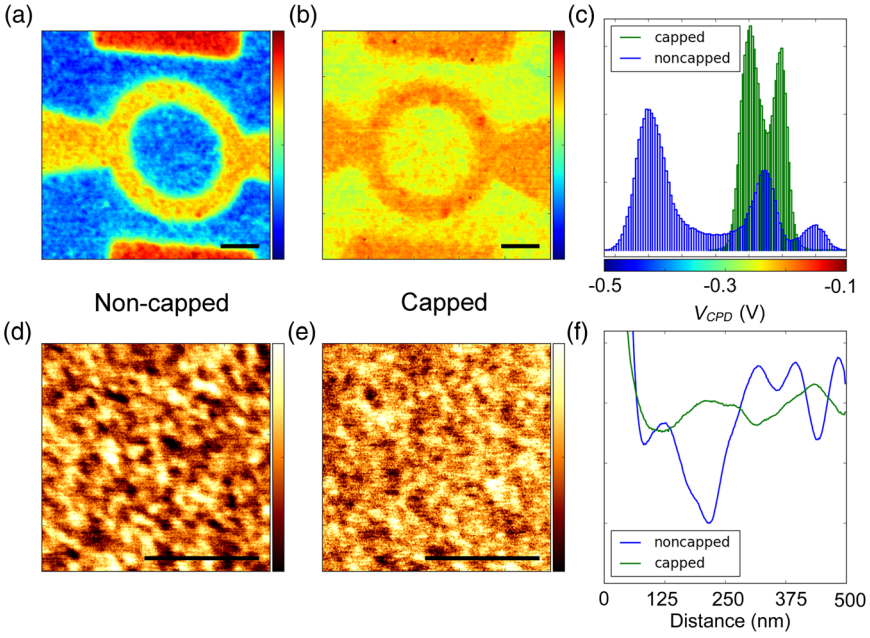

FIG. 4. ImEFM images of the contact potential difference V_{CPD} of both noncapped [(a) and (d)] and capped [(b) and (e)] structures. The space bar in all images is 500 nm. Image histograms (c) show a much higher contrast in the noncapped structure. Higher-resolution scans [(d) and (e)] of the conducting lead region of each structure reveal the inhomogeneity of V_{CPD}, where the radial autocorrelation function (f) indicates a characteristic size of the variations in the range 130 nm in the noncapped sample. In (a) and (b), the color scale ranges between −0.5 and −0.1 V, in (d) it ranges between −0.25 and −0.19 V, and in (e) it ranges between −0.20 and −0.16 V.

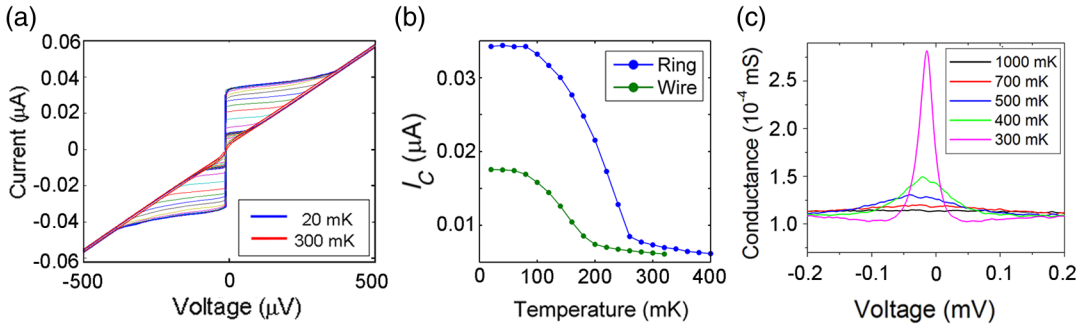

FIG. 5. Superconducting properties of SCO-capped nanostructures: (a) current-voltage characteristics of a 100-nm ring as a function of the temperature (in 20-mK steps), (b) critical current versus the temperature for a ring and a wire with the same width (100 nm), and (c) conductance versus the voltage above a critical temperature of a 100-nm ring.

explaining the temperature dependence of the carrier concentration in our samples.

We also show that the electrical-transport properties of a SCO-capped interface are similar in devices with dimensions ranging from 100 nm to 30 μm, which may be important for applications demanding small structures. In contrast, the sheet resistance shows a significant increase in structures with dimensions below 1 μm for noncapped interfaces. We previously argued that this effect can be related to a presence of lateral inhomogeneity in the q2DEG [18]. We note that, while the room-temperature sheet resistance is increased in noncapped nanostructures, they never become insulating. We may interpret this lack of insulating behavior as the presence of two different regions with high and low electrical conductivity, which is in line with a recent model of two types of carriers with low and high effective masses [14]. The two-region interpretation is further supported by the carrier freeze-out observed in noncapped samples. Nanopatterned noncapped samples (room-temperature measurements reported in Fig. 2) show an increase of the resistivity above our measurement limit when cooled down to a low temperature. This freeze-out affects small structures with transverse dimensions comparable to the average size of a low-conductivity region, approximately 130 nm as observed in the surface potential images. The size of the lateral inhomogeneity is estimated from scaling arguments to be around 100 nm [17], also in good agreement with our results.

We also observe a superconducting transition in SCO-capped interfaces. This is in contrast to the previously reported absence of superconductivity down to 60 mK in SCO-capped interfaces [19]. Superconductivity in the LAO/STO interface is believed to originate from the STO substrate [4,5]. The critical temperature of doped STO follows a domelike behavior as a function of the bulk carrier concentration [27]. Therefore, different behavior can be explained as different doping in the LAO/STO interface. The sheet-carrier concentration in our samples is about 2 times higher than that reported in Ref. [19] (2×10^{13} and 1×10^{13} cm^{-2}, correspondingly). Assuming a reasonable estimation of the thickness of the superconducting layer of about 10 nm [10], a corresponding bulk carrier concentration in our samples is about 2×10^{19} cm^{-3}. The optimal carrier concentration in STO is about 10^{20} cm^{-3} corresponding to a maximum critical temperature of about 0.3 K [27,28]. This means that our samples are underdoped, and a small deviation of the carrier concentration may bring the system into the nonsuperconducting regime. Moreover, a comparison between different interfaces is complicated by the uncertainty in the thickness of the conducting layer. The superconducting transition appears between 0.2 and 0.3 K in our samples, but the I–V characteristics show nonlinear behavior even above the "bulk" critical temperature [see Fig. 5(b)]. The nonlinear shape of the I–V characteristics is reminiscent of a network of resistively shunted Josephson junctions. Remnants of this nonlinearity are observed at a temperature up to 700 mK, which may be interpreted as indicating superconductivity at higher temperatures. Two-gap superconductivity is theoretically predicted [29] and experimentally observed [15,16] in STO. While there is no general agreement on an interpretation, these data may indicate the presence of a percolative superconducting transition in the LAO/STO interface, related to the presence of two types of carriers with low and high effective mass [16]. An alternative interpretation is suggested in Ref. [15] as due to a preformation of Cooper pairs above the critical temperature.

ImEFM imaging provides more insight into the inhomogeneous nature of the q2DEG (see Fig. 4). The clear contrast in the surface potential between insulating and conductive parts of nanostructures in ImEFM images proves that the electrical transport is indeed confined within patterned structures, ruling out the possibility that fabrication errors can be a cause of spread in electrical-transport properties in noncapped nanostructures [Figs. 4(a) and 4(b)]. The inhomogeneous V_{CPD} images observed in the conducting regions of both capped and noncapped interfaces have a correlation length that agrees well with the estimations of the size of puddles discussed above. ImEFM images the variation in the work function of the interfacial

layer, reflecting local changes in the Fermi energy E_F. Within the free-electron model with diffusive transport, a variation in E_F reflects a change in the concentration and, thereby, conductivity. Therefore, the contrast in the surface potential can be interpreted as due to the presence of islands with different resistivity. This is further supported by the fact that a similar contrast appears in two types of samples with different surface layers (LAO film in noncapped samples and STO film in capped ones). It is interesting to notice that there is a difference in inhomogeneity between the uncapped and SCO-capped samples, but it is smaller than one would first expect taking into account the different results on electrical-transport properties. The exact microscopic nature of these inhomogeneities is not known; it can be due to a variation of the LAO film stoichiometry [11], oxygen vacancies that tend to form clusters [13], or a lateral variation of the dielectric constants in the LAO film or STO substrate. Being able to quantify the change in the carrier density from the measured change in the Fermi energy would strengthen our findings, but this requires additional modeling and measurements that are beyond the scope of this paper. Even if we assume a free-electron model description for the Fermi energy, we get

$$dE/E = 2/3 \times dN/N, \tag{1}$$

where E is the Fermi energy and N is the electron density. With ImEFM, we measure the change dE, and we can say qualitatively that there is a corresponding change in carrier density dN. To quantify dN, we would need to independently measure (or model) the starting conditions E and N. Moreover, ImEFM does not measure directly E of the sample but the difference $E_{\text{sample}} - E_{\text{tip}}$. When we compare two scans (or two regions within one scan, or different puddles), we get

$$(E_1 - E_{\text{tip}}) - (E_2 - E_{\text{tip}}) = E_1 - E_2 = dE. \tag{2}$$

At the same time, it would not help to calibrate the work function of the AFM tip E_{tip}; in that case, we get an "absolute" measure of the Fermi energy relative to the vacuum level, while in Eq. (1) E is measured relative to the bottom of the conduction band.

The retention of electronic conductivity in LAO/STO nanostructures, thanks to the SCO capping layer, together with the evidence of a superconductive transition lays the foundation for future experiments aimed at the understanding and use of the different ordering phenomena in the two-dimensional electron gas. It has been argued that a combination of intrinsic ferromagnetic polarization with strong spin-orbit coupling can lead to chiral p-wave superconductivity in the LAO/STO interface [30]. Cooper pairs can acquire a finite pair momentum perpendicular to the direction of magnetic ordering in the presence of strong spin-orbit coupling [31]. In this consideration, the LAO/STO interface is similar to the proposed p-wave superconductivity in semiconductor-superconductor heterostructures [32,33]. This could possibly lead to the realization of Majorana bound states in one-dimensional quantum wires [34]. A full comprehension of the interplay and competitions between the different electronic phases offer possibilities for the realization of topological superconducting states, which may be promising candidates for forthcoming applications, such as quantum computing.

V. CONCLUSIONS

Nanostructures with improved electrical-transport properties are fabricated at the LAO/STO interface with a SCO capping layer. The sheet resistance, charge-carrier density, and charge mobility in SCO-capped nanostructures are comparable with those measured at the micrometer scale, showing no dependence on the structure size. This can be interpreted as an improvement of the 2DEG lateral homogeneity in the capped samples. Surface potential imaging shows a more uniform surface potential and a larger characteristic size of the puddles in the capped samples. Superconductivity is shown in nanostructures of LAO/STO capped with SCO, together with a nonlinear I–V characteristic above the critical temperature.

ACKNOWLEDGEMENTS

This work was supported by the Swedish Research Council, the Knut and Alice Wallenberg Foundation, and the Swedish Institute Visby program. The support from the Swedish Infrastructure for Micro- and Nanofabrication-Myfab is appreciated.

[1] A. Ohtomo and H. Hwang, A high-mobility electron gas at $LaAlO_3/SrTiO_3$ heterointerface, Nature (London) **427**, 423 (2004).

[2] A. D. Caviglia, S. Gariglio, C. Cancellieri, B. Sacèpè, A. Fète, N. Reyren, M. Gabay, A. F. Morpurgo, and J.-M. Triscone, Two-Dimensional Quantum Oscillations of the Conductance at $LaAlO_3/SrTiO_3$ Interfaces, Phys. Rev. Lett. **105**, 236802 (2010).

[3] A. D. Caviglia, M. Gabay, S. Gariglio, N. Reyren, C. Cancellieri, and J.-M. Triscone, Tunable Rashba Spin-Orbit Interaction at Oxide Interfaces, Phys. Rev. Lett. **104**, 126803 (2010).

[4] N. Reyren *et al.*, Superconducting interfaces between insulating oxides, Science **317**, 1196 (2007).

[5] S. Gariglio, N. Reyner, A. D. Caviglia, and J.-M. Triscone, Superconductivity at the $LaAlO_3/SrTiO_3$ interface, J. Phys. Condens. Matter **21**, 164213 (2009).

[6] S. Thiel, G. Hammerl, A. Schmehl, C. W. Schneider, and J. Mannhart, Tunable quasi-two-dimensional electron gases in oxide heterostructures, Science **313**, 1942 (2006).

[7] L. Li, C. Richter, J. Mannhart, and R. Ashoori, Coexistence of magnetic order and two-dimensional superconductivity at $LaAlO_3/SrTiO_3$ interfaces, Nat. Phys. **7**, 762 (2011).

[8] C. Cen, S. Thiel, G. Hammerl, C. W. Schneider, K. E. Andersen, C. S. Hellberg, J. Mannhart, and J. Levy, Nanoscale control of an interfacial metal-insulator transition at room temperature, Nat. Mater. **7**, 298 (2008).

[9] D. Stornaiuolo, S. Gariglio, N. J. Couto, A. Fete, A. D. Caviglia, G. Seyfath, D. Jaccard, A. F. Morpurgo, and J.-M. Triscone, In-plane electronic confinement in superconducting $LaAlO_3/SrTiO_3$ nanostructures, Appl. Phys. Lett. **101**, 222601 (2012).

[10] N. Reyren, S. Gariglio, A. D. Caviglia, D. Jaccard, T. Schneider, and J.-M. Triscone, Anisotropy of the superconducting transport properties of the LAO/STO interface, Appl. Phys. Lett. **94**, 112506 (2009).

[11] A. S. Kalabukhov, Y. A. Boikov, I. T. Serenkov, V. I. Sakharov, V. N. Popok, R. Gunnarsson, J. Borjesson, N. Ljustina, E. Olsson, D. Winkler, and T. Claeson, Cationic Disorder and Phase Segregation in $LaAlO_3/SrTiO_3$ Heterointerfaces Evidenced by Medium-Energy Ion Spectroscopy, Phys. Rev. Lett. **103**, 146101 (2009).

[12] J. A. Bert, B. Kalisky, C. Bell, M. Kim, Y. Hikita, H. Y. Hwang, and K. A. Moler, Direct imaging of the coexistence of ferromagnetism and superconductivity at the $LaAlO_3/SrTiO_3$ interface, Nat. Phys. **7**, 767 (2011).

[13] N. Mohanta and A. Taraphder, Oxygen vacancy clustering and pseudogap behaviour at the $LaAlO_3/SrTiO_3$ interface, J. Phys. Condens. Matter **26**, 215703 (2014).

[14] S. Caprara, D. Bucheli, N. Scopigno, N. Bergeal, J. Biscaras, S. Hurand, J. Lesueuer, and M. Grilli, Inhomogeneous multi carrier superconductivity at $LaXO_3/SrTiO_3$ (X = Al or Ti) oxide interfaces, Supercond. Sci. Technol. **28**, 014002 (2015).

[15] C. Richter, H. Boschker, W. Dietsche, E. Fillis-Tsirakis, R. Jany, F. Loder, L. F. Kourkoutis, D. A. Muller, J. R. Kirtley, C. W. Schneider, and J. Mannhart, Interface superconductor with gap behaviour like a high-temperature superconductor, Nature (London) **502**, 528 (2013).

[16] D. Bucheli, S. Caprara, and M. Grilli, Pseudo-gap as a signature of inhomogeneous superconductivity in oxide interfaces, Supercond. Sci. Technol. **28**, 045004 (2015).

[17] S. Caprara, J. Biscaras, N. Bergeal, D. Bucheli, S. Hurand, C. Feuillet-Palma, A. Rastogi, R. C. Budhani, J. Lesueur, and M. Grilli, Multiband superconductivity and nanoscale inhomogeneity at oxide interfaces, Phys. Rev. B **88**, 020504 (2013).

[18] P. P. Aurino, A. Kalabukhov, N. Tuzla, E. Olsson, T. Claeson, and D. Winkler, Nano-patterning of the electron gas at the $LaAlO_3/SrTiO_3$ interface using low-energy ion beam irradiation, Appl. Phys. Lett. **102**, 201610 (2013).

[19] M. Huijben, G. Koster, M. K. Kruize, S. Wenderich, J. Verbeeck, S. Bals, E. Slooten, B. Shi, H. Molegraaf, J. E. Kleibeuker, S. van Aert, J. B. Goedkoop, A. Brinkman, D. H. A. Blank, M. S. Golden, G. van Tendeloo, H. Hilgenkamp, and G. Rijnder, Defect engineering in oxide heterostructures by enhanced oxygen surface exchange, Adv. Funct. Mater. **23**, 5240 (2013).

[20] M. Kawasaki, K. Takahashi, T. Maeda, R. Tsuchiya, M. Shinohara, O. Ishiyama, T. Yonezawa, M. Yoshimoto, and H. Koinuma, Atomic control of the $SrTiO_3$ crystal surface, Science **266**, 1540 (1994).

[21] G. Koster, B. L. Kropman, G. J. H. M. Rijnders, D. H. A. Blank, and H. Rogalla, Quasi-ideal strontium titanate crystal surfaces through formation of strontium hydroxide, Appl. Phys. Lett. **73**, 2920 (1998).

[22] D. B. Chrisey and G. K. Hubler, *Pulsed Laser Deposition of Thin Films* (Wiley, New York, 1994).

[23] A. Ichimiya and P. I. Cohen, *Reflection High Energy Electron Diffraction* (Cambridge University Press, Cambridge, England, 2004).

[24] See Supplemental Material at http://link.aps.org/supplemental/10.1103/PhysRevApplied.6.024011 for the *in situ* RHEED during sample deposition and for a detailed investigation of the effects of low-energy Ar irradiation on SCO-capped samples.

[25] P. P. Aurino, A. Kalabukhov, N. Tuzla, E. Olsson, A. Klein, P. Erhart, Y. A. Boikov, I. T. Serenkov, V. I. Sakharov, T. Claeson, and D. Winkler, Reversible metal-insulator transition of Ar-irradiated $LaAlO_3/SrTiO_3$ interfaces, Phys. Rev. B **92**, 155130 (2015).

[26] R. Borgani, D. Forchheimer, J. Bergqvist, P.-A. Thorén, O. Inganas, and D. Haviland, Intermodulation electrostatic force microscopy for imaging surface, Appl. Phys. Lett. **105**, 143113 (2014).

[27] C. S. Koonce, M. L. Cohen, J. F. Schooley, W. R. Hosler, and E. R. Pfeiffer, Superconducting Transition Temperatures of Semiconducting $SrTiO_3$, Phys. Rev. **163**, 380 (1967).

[28] J. F. Schooley, H. P. R. Frederikse, W. R. Hosler, and E. R. Pfeiffer, Superconductive Properties of Ceramic Mixed Titanates, Phys. Rev. **159**, 301 (1967).

[29] R. M. Fernandes, J. T. Haraldsen, P. Wolfle, and A. V. Balatsky, Two-band superconductivity in doped $SrTiO_3$ films and interfaces, Phys. Rev. B **87**, 014510 (2013).

[30] L. Fidkowski, H.-C. Jiang, R. M. Lutchyn, and C. Nayak, Magnetic and superconducting ordering in one-dimensional nanostructures at the $LaAlO_3/SrTiO_3$ interface, Phys. Rev. B **87**, 014436 (2013).

[31] N. Pavlenko, T. Kopp, E. Y. Tsymbal, G. A. Sawatzky, and J. Mannhart, Magnetic and superconducting phases at the $LaAlO_3/SrTiO_3$ interface: The role of interfacial Ti 3d electrons, Phys. Rev. B **85**, 020407 (2012).

[32] J. D. Sau, R. M. Lutchyn, S. Tewari, and S. Das Sarma, Generic New Platform for Topological Quantum Computation Using Semiconductor Heterostructures, Phys. Rev. Lett. **104**, 040502 (2010).

[33] R. M. Lutchyn, J. D. Sau, and S. Das Sarma, Majorana Fermions and a Topological Phase Transition in Semiconductor-Superconductor Heterostructures, Phys. Rev. Lett. **105**, 077001 (2010).

[34] Y. Oreg, G. Refael, and F. von Oppen, Helical Liquids and Majorana Bound States in Quantum Wires, Phys. Rev. Lett. **105**, 177002 (2010).